

Performance of the ATLAS Liquid Argon Calorimeter after Three Years of LHC Operation and Plans for a Future Upgrade

Nikiforos Nikiforou, on behalf of the ATLAS Collaboration

Abstract—The ATLAS experiment is designed to study the proton-proton collisions produced at the Large Hadron Collider (LHC) at CERN. Liquid argon sampling calorimeters are used for all electromagnetic calorimetry as well as hadronic calorimetry in the endcaps. After installation in 2004–2006, the calorimeters were extensively commissioned over the three-year period prior to first collisions in 2009, using cosmic rays and single LHC beams. Since then, approximately 27 fb^{-1} of data have been collected at an unprecedented center of mass energy. During all these stages, the calorimeter and its electronics have been operating almost optimally, with a performance very close to specifications. This paper covers all aspects of these first years of operation.

The excellent performance achieved is especially presented in the context of the discovery of the elusive Higgs boson. The future plans to preserve this performance until the end of the LHC program are also presented.

Index Terms—Calorimetry.

I. INTRODUCTION

THE ATLAS detector [1] is one of the two large general-purpose experiments designed to study proton-proton as well as heavy-ion collisions at the CERN Large Hadron Collider (LHC). Inside the LHC, bunches of up to 10^{11} protons collide nominally every 25 ns to provide proton-proton collisions at a design luminosity of $10^{34} \text{ cm}^{-2}\text{s}^{-1}$ and a center of mass energy up to 14 TeV. For its first years of operation, the LHC has been operating at a reduced center of mass energy, namely 7 TeV in 2011 and 8 TeV in 2012, and at an increased 50 ns bunch spacing. Already operating close to its design luminosity, the LHC creates an extremely challenging environment for the experiments, by producing multiple interactions per bunch crossing (*pileup*), high radiation doses and high particle multiplicities at unprecedented energies.

The dimensions of the detector (Fig. 1) are 25 m in height and 44 m in length. The overall weight of the detector is approximately 7000 tonnes and it is housed in an underground experimental cavern at Point-1 near the CERN main site. It covers nearly the entire solid angle around the collision point, and successively consists of an Inner tracking Detector (ID) surrounded by a thin superconducting solenoid, electromagnetic (EM) and hadronic calorimeters, and a muon spectrometer incorporating three large toroidal magnet systems.

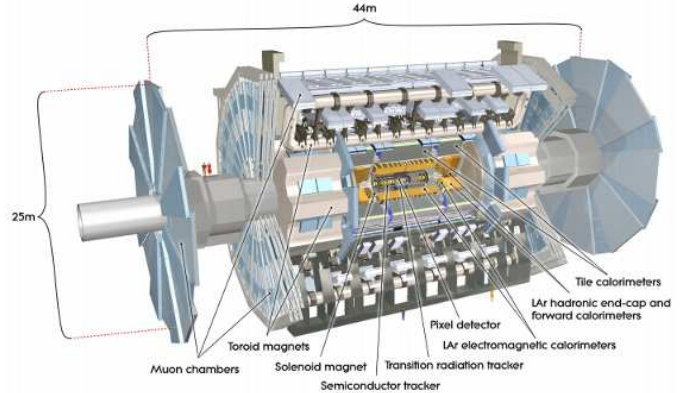


Fig. 1. Cut-away view of the ATLAS detector [1].

The ATLAS calorimeter system covers the pseudorapidity¹ range $|\eta| < 4.9$ and provides energy measurements of particles. Sampling calorimeters based on Liquid Argon (LAr) technology are used for the detection of electromagnetic (EM) objects like electrons and photons up to $|\eta| = 3.2$, as well as hadronic objects in the $|\eta|$ range 1.5 – 4.9. The LAr calorimeter system (Fig. 2) is the subject of this paper and is described in more detail later. Hadronic calorimetry within $|\eta| < 1.7$ is provided by a steel/scintillator-tile calorimeter.

II. THE ATLAS LAR CALORIMETER SYSTEM

In ATLAS, EM calorimetry is provided by barrel ($|\eta| < 1.475$) and endcap ($1.375 < |\eta| < 3.2$) accordion geometry lead/LAr sampling calorimeters. An additional thin LAr presampler covering $|\eta| < 1.8$ allows corrections for energy losses in material upstream of the EM calorimeters. The barrel electromagnetic (EMB) calorimeter [2] consists of two half-barrels housed in the same cryostat. The electromagnetic endcap calorimeter (EMEC) [3] comprises two wheels, one on each side of the EM barrel. The wheels are contained in independent endcap cryostats together with the hadronic endcap and forward calorimeters described later. The wheels themselves consist of two co-axial wheels, with the outer

¹ATLAS uses a right-handed coordinate system with its origin at the nominal interaction point (IP) in the center of the detector and the z -axis along the beam pipe. The x -axis points from the IP to the center of the LHC ring, and the y -axis points upward. Cylindrical coordinates (r, ϕ) are used in the transverse plane, ϕ being the azimuthal angle around the beam pipe. The pseudorapidity is defined in terms of the polar angle θ as $\eta = -\ln \tan(\theta/2)$. In ATLAS, the so-called “side-A” refers to positive z -values while “side-C” refers to the negative side.

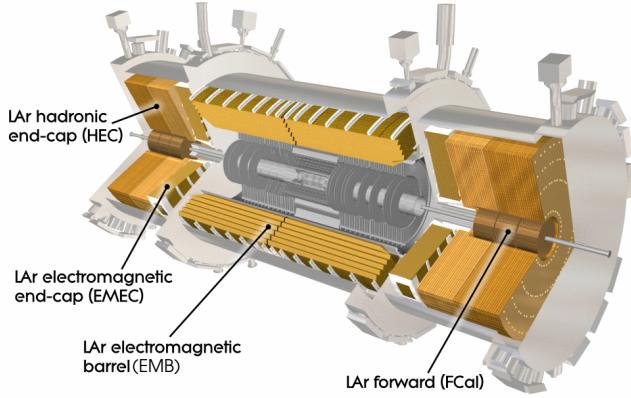


Fig. 2. The ATLAS LAr calorimeter system [1].

wheel (OW) covering the region $1.375 < |\eta| < 2.5$ and the inner wheel (IW) covering the region $2.5 < |\eta| < 3.2$.

The hadronic calorimetry provided by the tile calorimeter is complemented by two parallel-plate copper/LAr hadronic endcap (HEC) calorimeters [4] that cover the region $1.5 < |\eta| < 3.2$. Each HEC consists of two independent wheels which combined provide 4 longitudinal calorimeter layers.

Finally, the forward calorimeters (FCal) [5] provide coverage over $3.1 < |\eta| < 4.9$. In order to withstand the high particle fluxes in this region, they are based on a novel design that uses cylindrical electrodes consisting of rods positioned concentrically inside tubes parallel to the beam axis, supported by a metal matrix. Very narrow LAr gaps have been chosen to avoid ion buildup at high rates and the gap is kept constant with a winding fiber wrapped around the rods. Three cylindrical modules comprise the FCal, arranged sequentially; the module closest to the IP is optimized for EM measurements and uses mainly copper as absorber and 269 μm gaps. The two subsequent modules are made mainly of tungsten and are optimized for hadronic measurements with gaps of 375 and 500 μm respectively.

In total, the LAr calorimeter system comprises 8 subsystems (EMBA, EMBC, EMECA, EMECC, HECA, HECC, FCalA and FCalC) collectively referred to as *partitions*.

A. Design and Principle of Operation

The EM calorimeters comprise accordion-shaped copper-kapton electrodes positioned between lead absorber plates and kept in position by honeycomb spacers while the system is immersed in LAr (Fig. 3). Incident particles shower in the absorber material and subsequently the LAr is ionized. Under the influence of the electric field between the grounded absorber and powered electrode, the ions and electrons drift, the latter inducing a triangular pulse (Fig. 4) to be collected by the electrodes. With the purpose of redundancy, both sides of the electrodes are powered independently which allows for the collection of half of the signal should one side lose power.

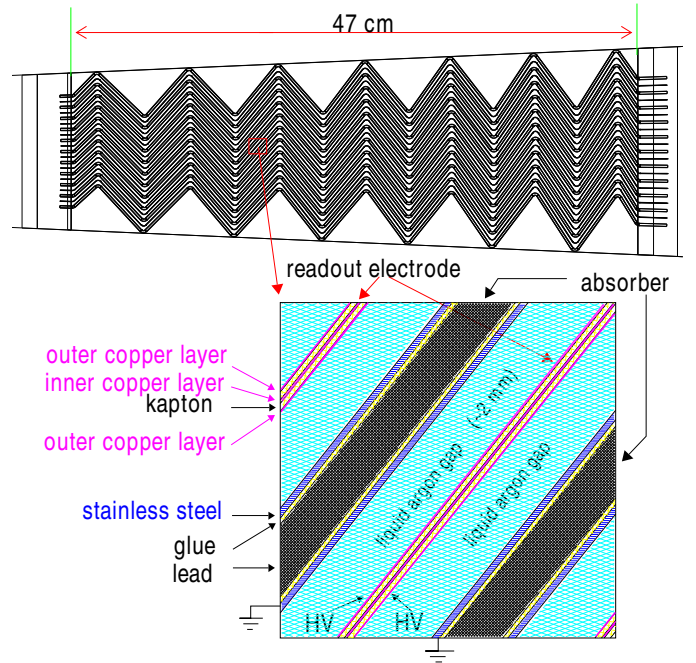


Fig. 3. Accordion structure of the barrel. The top figure is a view of a small sector of the barrel calorimeter in a plane transverse to the LHC beams [6].

In the EMB, the size of the drift gap on each side of the electrode is 2.1 mm, which corresponds to a total electron drift time [6] of approximately 450 ns for a nominal operating voltage of 2000 V. In the EMEC, the gap is a function of radius and therefore the HV varies with η to provide a uniform detector response. To facilitate installation, the absorbers and electrodes are ganged in ϕ -modules. For most of the EM calorimeter, EMB and EMEC-OW, each module has three layers in depth with different granularities, as can be seen in Fig. 5, while each EMEC-IW module has only two layers. The EM calorimeter is designed so the largest fraction of the energy is collected in the second layer while the back layer collects only the tail of the EM shower. Using the energy measurement and position for all cells in all layers of the calorimeter contained in the shower, the incident particle energy can be reconstructed and, taking advantage of the fine segmentation of the first layer, its direction and characteristics can be inferred. As discussed later, the fine segmentation is extremely useful in the discrimination between photons and jets with a leading π^0 meson which primarily decays to two photons. In addition, with its novel pointing geometry, the calorimeter can reconstruct the direction of neutral particles, such as photons, for which semiconductor tracking cannot be used.

The principle of operation is similar for the HEC and FCal, though the design details, gap size, HV and drift time characteristics are different and vary with position.

B. Readout

The ionization signals from all the cells are led outside the cryostats via 114 feedtroughs. Front End Boards (FEBs) [7] housed in crates mounted directly on the feedtroughs, receive

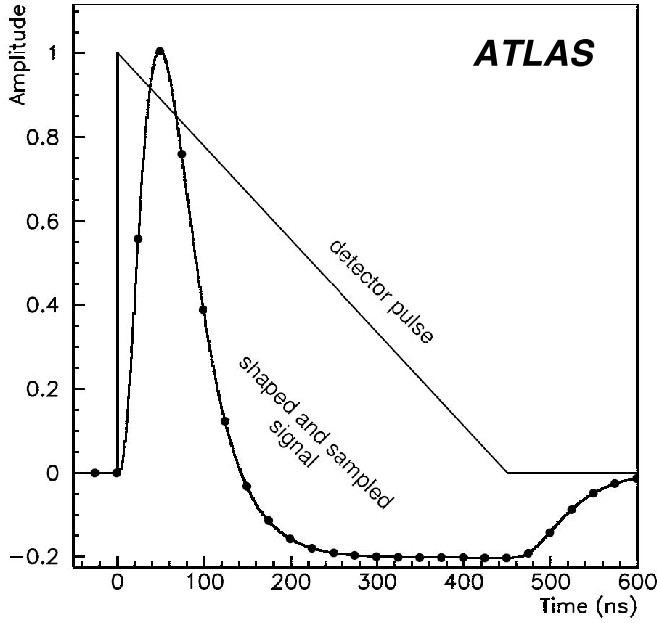


Fig. 4. Shapes of the LAr calorimeter current pulse in the detector and of the signal output from the shaper chip. The dots indicate an ideal position of samples separated by 25 ns [1].

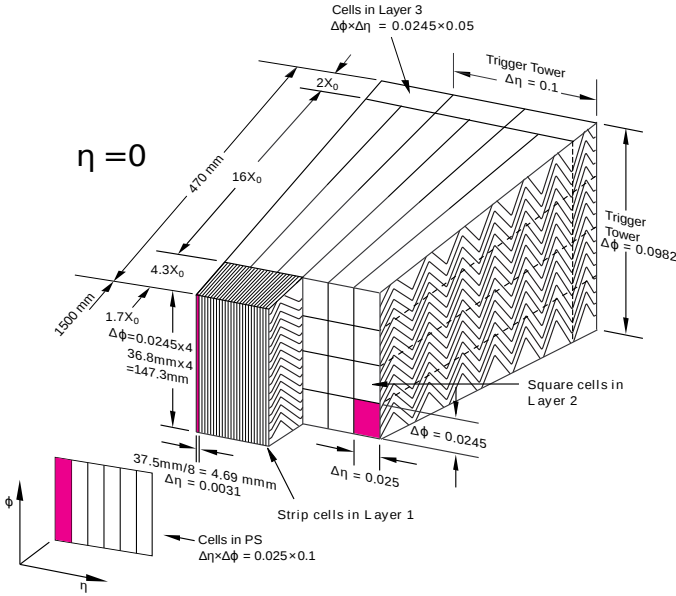


Fig. 5. Sketch of an EMB module where the different layers are visible. The granularity in eta and phi of the cells of each of the three layers and of the trigger towers is also shown [1].

the raw signals from up to 128 calorimeter channels, process, digitize and transmit samples via optical link (see Fig. 6) to the Back-End electronics housed outside the experimental cavern. The signal for each channel is split into three overlapping linear gain scales (Low, Medium and High) in the approximate ratio 1/9/80, in order to meet the large dynamic range requirements for the expected physics signals. For each gain, the triangular pulse is shaped (Fig. 4) with a bipolar $CR - (RC)^2$ analog filter to optimize the signal-to-noise ratio. The shaped signals are then sampled at the LHC bunch-crossing frequency

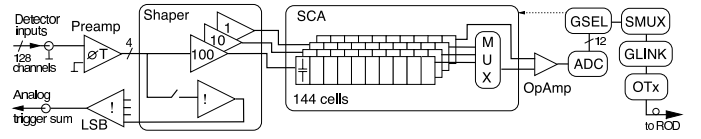


Fig. 6. Front End Board block diagram [1].

of 40 MHz and the samples for each gain are stored in a Switched Capacitor Array (SCA) analog memory buffer while waiting for a Level-1 (L1) trigger accept. For events accepted by the trigger, the optimal gain is selected for each channel, and the samples are digitized and transmitted. In 2011 and 2012, typically 5 samples were digitized for each pulse, whereas for the upcoming 14 TeV run, reducing the number of samples per pulse to 4 is being considered.

In addition to the FEBs, the Front End Crates house several additional boards. Tower Builder Boards facilitate the propagation of information to the trigger processor by summing calorimeter cells in all layers in “trigger towers” with a size of approximately 0.1×0.1 in $\Delta\eta \times \Delta\phi$. Calibration Boards allow the calibration of the electronics by injecting a known exponential pulse to simulate the LAr ionization signal. The calibration signals are then reconstructed through the regular readout chain. Finally, auxiliary boards perform service tasks such as clock distribution, communication and monitoring.

C. Cell Energy and Time Reconstruction

The optimal filtering [8] technique is used to reconstruct the cell energy and peaking time from the samples of the shaped calorimeter pulse. The procedure described here applies to all LAr subsystems though it differs slightly in the case of the FCal. To calculate the cell energy, E_{cell} in MeV, from the samples s_j in ADC counts, the following formula is used:

$$E_{\text{cell}} = F_{\mu A \rightarrow \text{MeV}} \cdot F_{\text{DAC} \rightarrow \mu A} \cdot \frac{1}{\frac{M_{\text{phys}}}{M_{\text{cali}}}} \cdot R \sum_{j=1}^{N_{\text{samples}}} a_j (s_j - p)$$

while to calculate the time a similar formula is used:

$$t_{\text{cell}} = \frac{1}{E_{\text{cell}}} \sum_{j=1}^{N_{\text{samples}}} b_j (s_j - p)$$

where $F_{\mu A \rightarrow \text{MeV}}$ is a coefficient that is obtained from test beam studies and converts the ionization current values to energy values, $F_{\text{DAC} \rightarrow \mu A}$ is a property of the calibration board and $\frac{M_{\text{phys}}}{M_{\text{cali}}}$ is a factor to correct for differences between the physics signal and calibration pulses. R is the ramp slope and p is the pedestal (electronic baseline) obtained from calibration. The parameters a_j and b_j are sets of Optimal Filtering Coefficients calculated from the knowledge of the calibration pulse shape and the noise autocorrelation function, to give the optimal energy and time resolution. Finally, a *Quality Factor*, Q^2 , is calculated for each cell, as an estimate of the quality of the reconstructed pulse.

III. OPERATION

In order to meet the performance requirements, a significant effort is made by the LAr Operations group to continuously

monitor the detector status and performance and take corrective actions if needed. This task is supported by various monitoring systems conceived and installed for this purpose. A Detector Control System (DCS) has been developed in the ATLAS-wide DCS framework to provide control, monitoring and human interface with the hardware, based on the commercial SCADA software PVSS-II (now named SIMATIC WinCC Open Architecture) [9].

A. Cryogenic System Stability

The cryogenic system aims to provide stable LAr conditions. The temperature sensitivity of the LAr calorimeter has been determined to follow a linear relationship with a 2% decrease of the measured signal per kelvin. This includes the contribution from LAr density variations with temperature as well as drift velocity variations, contributing to changes of $-0.45\%/K$ and $-1.55\%/K$ respectively. In order to meet the design energy resolution, a 100 mK temperature stability and uniformity is required.

A temperature monitoring system is in place to monitor and log the conditions so as to be able to correct for any temperature variations and non-uniformities. The temperature monitoring system comprises more than 400 calibrated precision temperature probes (PT100 platinum resistors) distributed throughout the three cryostats and immersed in the LAr. Measurements are taken every minute and a conditions database is updated if there is a change from the previous measurement.

Periodic studies are performed to monitor the stability of the cryogenic system during data taking. Temperature data are collected over long periods of time without interventions on the cryogenic system and low voltage power supply and for constant general conditions, such as the magnetic field. Fig. 7 shows the temperature uniformity of the LAr barrel calorimeter, demonstrating an overall barrel temperature uniformity of 59 mK for data collected over a period of 10 days. Similar or better results are obtained in the endcaps, satisfying the design requirements. Finally, Fig. 8 shows the distribution of the RMS of the temperature measurements for each of the temperature probes in the LAr calorimeter cryostats, over the same period. The average RMS of 1.5 mK demonstrates the reliability of the temperature control and monitoring system.

An additional source of non-uniformity in the cryogenic system arises from the presence of impurities in the LAr. Ionization signal electrons can attach to electronegative impurities, such as O_2 , which would lead to the degradation of the signal measurement. A limit of 1000 ppb oxygen impurities or equivalent has been set for the efficient operation of the calorimeter.

The stability of the LAr purity is monitored in 10 to 15 minute intervals by a system of 30 purity monitors [11] installed throughout the cryostats. Each purity monitor measures the deposition of known charges from two contained monoenergetic radioactive sources (^{207}Bi and ^{241}Am) in ionization chambers. The monitors were shown to have a systematic uncertainty of 19% and a statistical uncertainty for a single measurement of ~ 5 ppb. Fig. 9 shows the impurity levels over the course of two years between July 2007 and July 2009 for

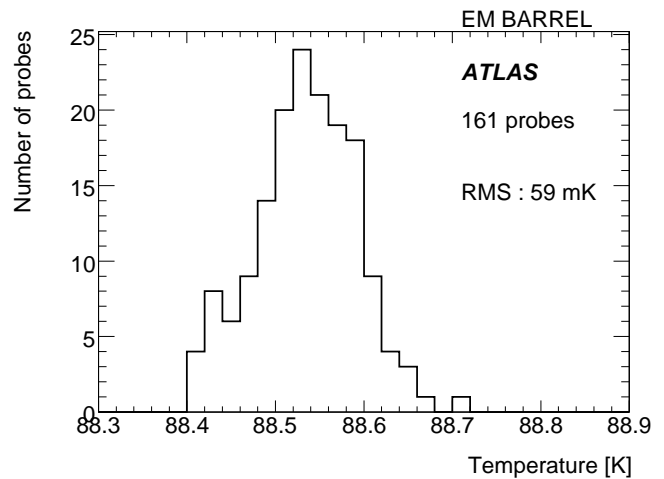


Fig. 7. Distribution of the average temperature measured over ten days for temperature probes within the EM Barrel cryostat [10].

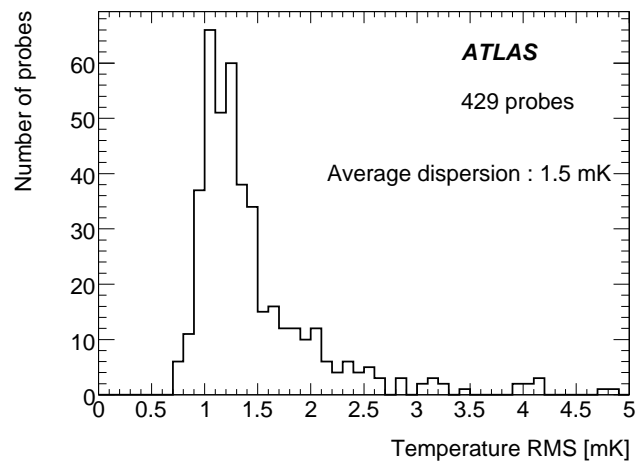


Fig. 8. Distribution of the RMS of the temperature measurements, over ten days, for each of the temperature probes within all three of the LAr calorimeter cryostats [10].

HECA. The overall levels of impurities have been measured to be approximately 200 ppb and 140 ppb in the barrel and endcap cryostats respectively, well below the operational limit. Finally, the levels have been shown to be stable except in the case of side C of the endcap where a small degradation of approximately 5 ppb per year is observed.

B. High Voltage Operation

The high voltage (HV) system provides the electric field so that the ionization signal propagates to the measurement electrodes for readout. The HV values are monitored in real time via the DCS system and stored in a conditions database. Suitable corrections are applied during the energy reconstruction for any deviations from the nominal values.

During data taking, some HV hardware modules may trip, which leads to loss of power to one side of an electrode, thereby inhibiting the signal measurement. Procedures have been established for the manual recovery of tripped HV lines on a case-by-case basis. In addition, an autorecovery

Purity HEC1/2 Side A

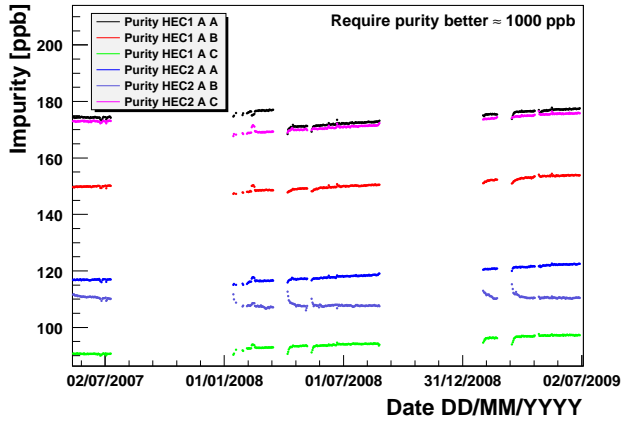


Fig. 9. Impurity levels in O_2 equivalents for HECA. Each point shows the mean of the purity values measured over a single day and excludes extreme or unreasonable values that can be attributed to instrumental effects [10].

LAr correction factors for reduced High Voltage

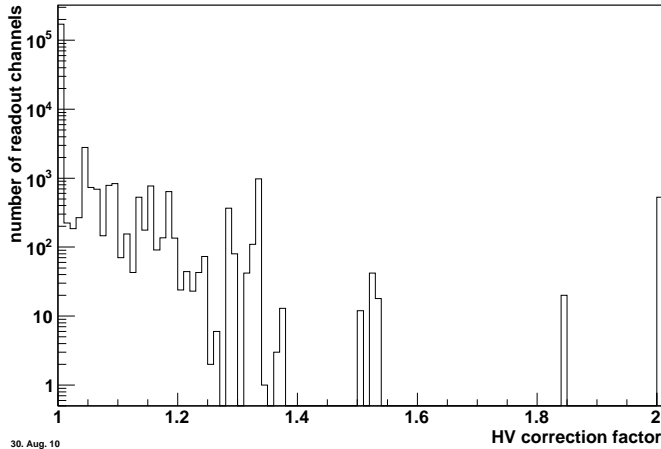


Fig. 10. Distribution of cell energy correction factors applied for channels serviced by at least one HV line operated at reduced voltage [12].

system has been implemented for modules that are not tripping systematically. Owing to the frequent measurement of the HV values, data recorded during the ramp-up of tripped lines can be corrected and used in analysis. Specialized studies were performed to verify that data collected during HV recovery can safely be used in analysis. During the trip itself, the rapid variation of the voltage makes the proper correction of the signal impractical, leading to a small loss of data. In order to limit the number of trips and minimize this inefficiency, problematic lines that trip frequently are set to lower operating HV values and a correction is applied for the energy of the affected cells. A typical distribution of correction factors is shown in Fig. 10. Finally, more robust HV modules have been deployed that allow the module to run in current control mode instead of tripping, which prevents the voltage drop. All the above improvements result in the minimization of data rejection due to HV trips in 2012 which was limited to 0.46%.

C. Electronics Calibration and Stability

Calibration campaigns are performed regularly and involve special runs in the absence of LHC beams to measure the response of the FEB electronics in situ for each of the three gains. An infrastructure has been deployed to facilitate the retrieval and processing of those runs, the extraction of calibration constants and their propagation to a conditions database.

Daily pedestal and noise levels for each channel are determined by “Pedestal” runs where the channel is triggered without signal injection. The pedestal is computed for each channel from the average over the triggers and the number of samples.

In order to determine the gain for each channel, “Ramp” runs are also taken on a daily basis. In these runs, each channel is pulsed several times with a set of predetermined calibration board DAC values, corresponding to input currents. For each DAC value, the resulting pulses are reconstructed and an average pulse shape is computed from which the peak ADC value is measured. Thus, the relationship between the DAC and ADC values is obtained for each channel and, by fitting it with a first order polynomial, the ramp slope R is calculated.

To demonstrate the excellent stability of the LAr electronics, Fig. 11 shows example stability plots for the pedestal and gain values with respect to time in 2012, for FEBs in the LAr EM calorimeters (EMB and EMEC) in High gain. For each FEB, the pedestal and gain average over all channels serviced by that board is calculated and plotted as a function of time. Compared to a reference value, the pedestal difference distribution has an RMS of 0.030 ADC counts, while the relative gain difference distribution has an RMS of 0.343 per mil. The stability is similar for the other LAr calorimeters (HEC and FCal) and in the other gains, with a pedestal difference RMS ranging from 0.022 to 0.029 ADC counts. Finally, the relative gain difference is distributed with an RMS between 0.316 and 0.343 per mil for the EM calorimeters, 0.657–0.814 per mil for the HEC and 0.046–0.086 per mil for the FCal.

Finally, “Delay” runs are taken weekly or as often as it is needed to reconstruct the pulse shape itself in detail. In this mode, for each calibration pulse, the channel is triggered several times with incremental delays of 1.04 ns. On each trigger, 32 samples are acquired at 40 MHz and the entire pulse is therefore effectively sampled at 1.04 ns, allowing reconstruction of the pulse shape with high precision. Each channel is further pulsed several times and the procedure is repeated to calculate an average pulse shape. The shape is used to extract the Optimal Filtering Coefficients that describe the shape and are used in the energy and time reconstruction from pulse samples as well as the calculation of the quality of the reconstructed pulse.

The values of the calibration constants are monitored for significant variations and are updated in the database typically once a month, or whenever there is a change in the system conditions.

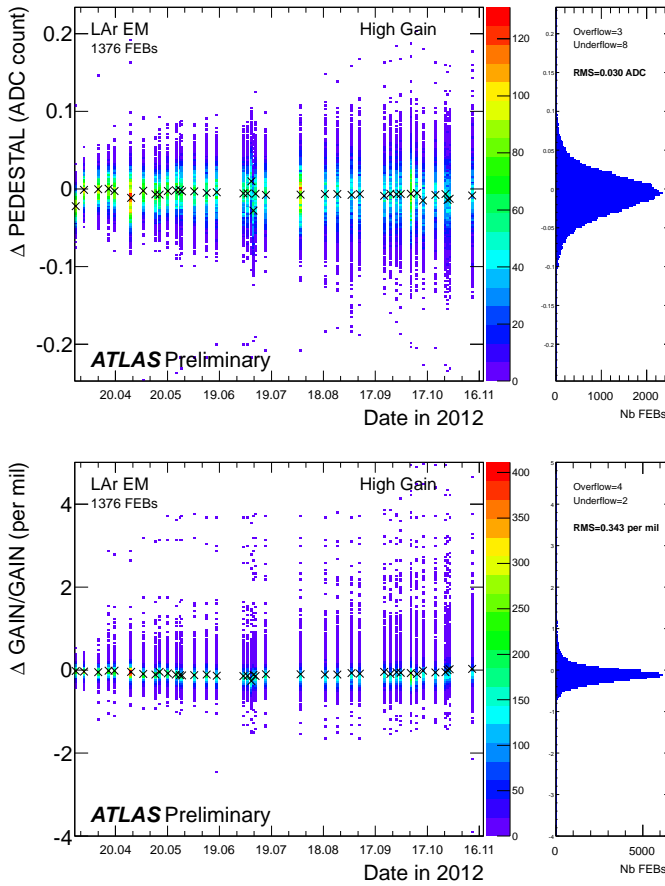


Fig. 11. Pedestal stability (top) and ramp stability (bottom) with respect to time in 2012 for the LAr EM calorimeters in High gain [10].

D. Timing

A precise timing measurement of calorimeter signals is particularly useful in the operation of the detector as well as physics analyses. Knowledge of time with a precision small compared to 25 ns (the nominal LHC bunch interval) is required to differentiate between energy deposits originating from collisions in the triggered bunch crossing as opposed to signals from neighboring bunch crossings. The latter phenomenon is known as “out-of-time pileup”. Further, excellent timing can be used to reject other sources of beam induced background such as satellite collisions and beam halo [13]. In addition, it provides a means to veto events with energy deposited by cosmic ray interactions overlapping with the triggered event. Finally, the timing can be employed in searches for new physics involving long-lived neutral particles decaying to photons [14], electrons or jets.

The timing measurement is performed with respect to the LHC clock phase delivered from a central system to ATLAS by means of an optical fiber. The clock phase can drift, for example, due to variations of the fiber length with temperature, and this can be detected by comparing with the actual bunch arrival times in ATLAS. The average time is monitored and is corrected for any global variations such as the LHC clock drift. In 2012, the capability to automatically compensate for any clock drift with a precision of a few tens of ps was

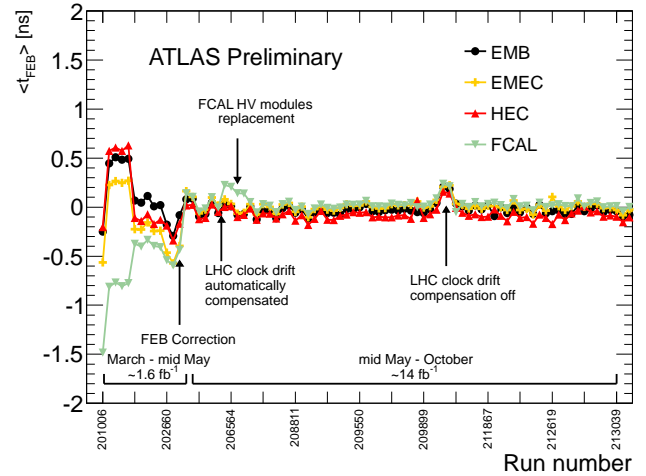


Fig. 12. Mean FEB time synchronization for each LAr partition [12].

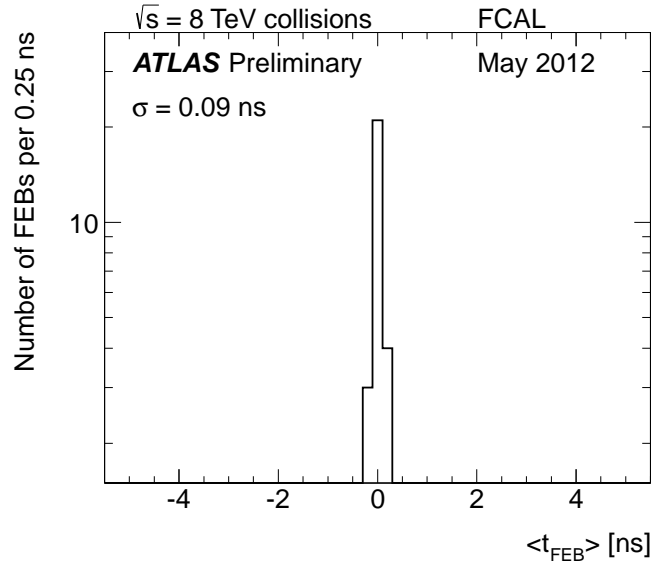


Fig. 13. Average time per Front End Board in the FCAL with 8 TeV collision data on May 2012 [12].

implemented during the June technical stop and performed very well as shown in Fig. 12.

The calorimeter is timed in with collision data with an online precision of approximately 1 ns. As shown in Fig. 13, the calorimeter is properly aligned and uniform in time, with a typical spread of the average FEB time between 0.09 ns and 0.17 ns, depending on the partition.

To improve the timing performance of the EM calorimeters further, a number of effects were studied and corrected for with good quality $W \rightarrow e\nu$ events. Additional calibration constants are computed as a function of the data taking period, FEB, channel within the FEB, cell energy and primary vertex position. After all constants are applied, a timing resolution of ≈ 290 ps is achieved for large energy depositions in the EMB, as shown in Fig. 14. By comparing the corrected time of the two electrons in $Z \rightarrow ee$ events, this resolution is understood to include a correlated contribution of ≈ 220 ps, expected to be

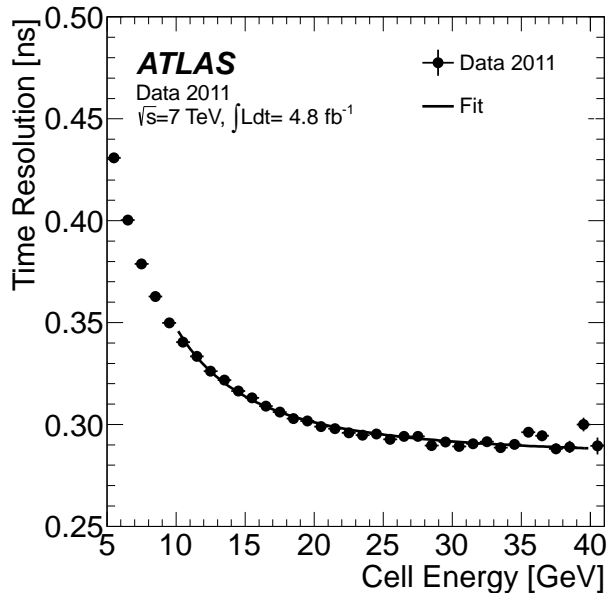


Fig. 14. Single cell time resolution energy dependence, for cells reconstructed in High gain, in the Middle layer of the LAr EM Barrel Calorimeter ($|\eta| < 1.4$). A fit with the expected energy dependence, comprising a so-called “noise term” and a “constant term”, added in quadrature, is shown superimposed [14].

dominated by the spread of the proton bunches along the LHC beamline, and an uncorrelated contribution of ≈ 190 ps. The latter component includes the intrinsic timing resolution of the LAr EMB and its readout, as well as residual non-uniformities and imperfections in the calibration procedure.

IV. DATA QUALITY MONITORING

A complex monitoring procedure was designed to track and quickly identify all potential problems affecting the detector, including the situations described in previous sections. The Data Quality Monitoring effort involves low level hardware monitoring via the DCS system as well as checks in every stage of the data acquisition and processing chain. Several algorithms assist trained personnel during the data taking (online monitoring) in detecting issues that could compromise data quality, so corrective actions can be taken. Offline, more detailed tests are performed using a subset of the recorded data which are expeditiously reconstructed to pinpoint blocks of data with suspected quality issues, or *defects*, before the processing of the bulk of the data is launched 48 hours later. The results of the tests are organized through a dedicated web infrastructure and trained experts decide on the defect type, localization, severity and length in time, with the ultimate goal of optimal detector efficiency. During this process, the detector conditions during the data taking, stored via DCS are also taken into account (for example HV values and status). The proposed actions are propagated as needed to the relevant conditions databases via automated procedures. After the bulk processing is completed, typically several days later, a final data quality assessment is performed to verify that the problems identified in the previous steps have been handled

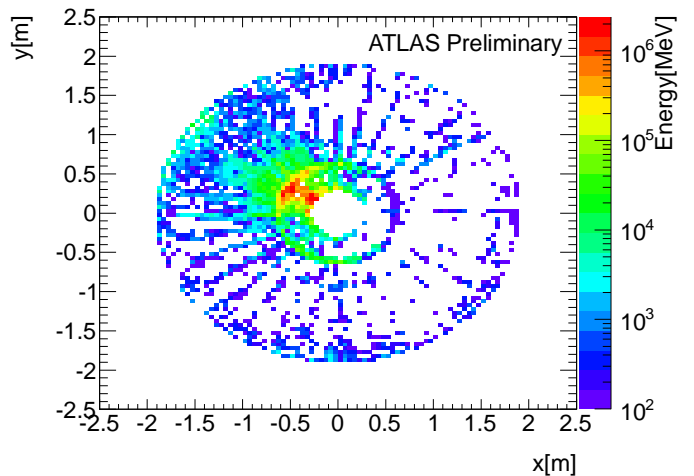


Fig. 15. Example of a single event affected by a noise burst recorded in empty LHC bunches in EMECA [12].

properly. If needed, the databases are further updated to flag the remaining issues and, if possible, to allow the recovery of data in future reprocessing.

A significant source of possible LAr inefficiency with an interesting pathology is the presence of bursts of large scale coherent noise, or *noise bursts*, mainly located in the endcaps. This phenomenon manifests itself only in the presence of collisions and was found to scale with instantaneous luminosity. The effect is very short in time, lasting usually less than $\sim 5 \mu\text{s}$, and during that time a significant percentage of channels exhibit signal readings which are significantly above the typical electronic noise levels. An example of such an event is shown in Fig. 15.

A useful variable for the description of noise burst events is $Y_{3\sigma}$ which represents the percentage of channels with a signal greater than three times the electronic noise measured during the LHC beam crossings without collisions (empty bunches). Hard noise burst events with large $Y_{3\sigma}$ are efficiently identified and flagged using the quality factors of the pulse measurements. However it was found that softer noise bursts, usually peripheral to a hard event and characterized by a $Y_{3\sigma}$ of the order 2-3%, are not efficiently flagged. Taking advantage of the short nature of the phenomenon, a *time window veto* procedure was established to identify these occurrences and reject neighboring events within a conservative time window around the identified noise burst. The window length was 1 s for 2011 and 250 ms for the 2012 data taking period. The efficiency of this method in rejecting large scale coherent noise events in empty bunches is demonstrated by Fig. 16.

The procedures described above were established and improved over the last few years of ATLAS operation and resulted in a continuous improvement in data quality and near optimal LAr efficiency. For 2012, the LAr inefficiency was limited to 0.88% of which 0.46% is due to HV trips while 0.2% is attributed to noise bursts.

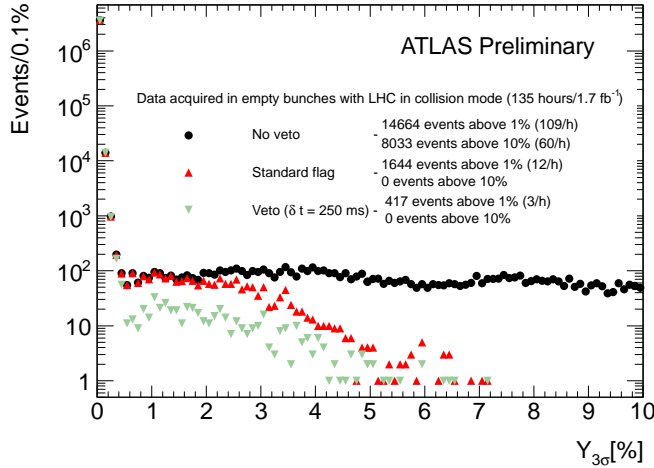


Fig. 16. Distribution of the percentage of noisy channels in the EM endcap, measured during empty bunches in LHC collision mode. The black points show the percentage without any corrective action. The red points represent the data after rejection of events identified by means of the quality factor only while the green points show the effect of the time veto procedure [12].

V. PHYSICS PERFORMANCE

While the low-level detector hardware and Data Quality monitoring are paramount to the successful running of the experiment, the ultimate goal is to reconstruct interesting physics events with efficiency, reliability and precision. It is the responsibility of the LAr calorimeter system to provide excellent measurements of physics objects, such as electrons, photons and jets, and contribute to the calculation of the event missing energy with high resolution. Tests at the physics level are performed continuously during the data taking periods using benchmark physics processes to gauge the object reconstruction stability and precision.

A. Energy Scale, Resolution and Stability

A detailed study was performed [15] to determine the electron performance of the ATLAS detector using the decays of the Z , W and J/ψ particles. The studies demonstrate the level of energy scale, resolution and uniformity of the LAr system as well the excellent overall performance of the ATLAS detector.

The EM showers that develop in the calorimeters are reconstructed as clusters of calorimeter cells that contain a large fraction of the deposited energy. Some energy is not contained in the cluster and some is lost before or after the calorimeter. For these reasons, corrections need to be applied. Calibration constants are calculated from MC simulation as a function of η , energy and shower depth. The overall energy scale is set with reconstructed mass distributions from $Z \rightarrow ee$ events (see Fig. 17 for an example in the barrel) and cross-checked using the electron E/p distribution in $W \rightarrow e\nu$ events. The latter takes advantage of the independent measurements of the electron energy, E in the calorimeter and its momentum, p in the Inner Detector (ID).

Having set the energy scale using the calibration constants, the calorimeter energy resolution can be studied. The resolu-

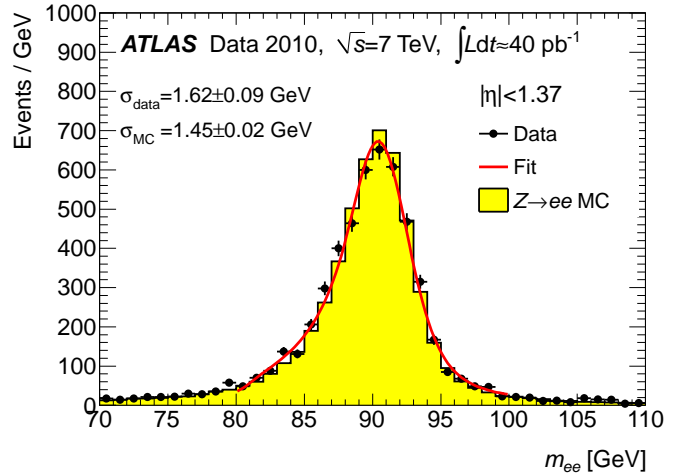


Fig. 17. Reconstructed dielectron mass distribution for $Z \rightarrow ee$ decays for $|\eta| < 1.37$ and comparison to simulation [15].

TABLE I
CALORIMETER ENERGY RESOLUTION CONSTANT TERM FOR ALL PARTITIONS

Subsystem	η -range	Effective constant term, c_{data}
EMB	$ \eta < 1.37$	$1.2\% \pm 0.1\%(\text{stat})^{+0.5\%}_{-0.6\%}(\text{syst})$
EMEC-OW	$1.52 < \eta < 2.47$	$1.8\% \pm 0.4\%(\text{stat}) \pm 0.4\%(\text{syst})$
EMEC-IW	$2.5 < \eta < 3.2$	$3.3\% \pm 0.2\%(\text{stat}) \pm 1.1\%(\text{syst})$
Fcal	$3.2 < \eta < 4.9$	$2.5\% \pm 0.4\%(\text{stat})^{+1.0\%}_{-1.5\%}(\text{syst})$

tion is usually parametrized with the following formula:

$$\frac{\sigma_E}{E} = \frac{a}{\sqrt{E}} \oplus \frac{b}{E} \oplus c$$

where a , b and c are η -dependent parameters called the *sampling term*, *noise term* and *constant term* respectively. Mass measurements in dielectron events, are compared to simulation and the lineshape of the J/ψ decay is used to verify that the sampling and noise terms are modeled correctly in simulation (Fig. 18). The width of the $Z \rightarrow ee$ decay mass distribution is then used to extract an *effective constant term*, c_{data} , including the calorimeter constant term as well as the effect of inhomogeneities and residual mis-calibration. For each η -range, the following formula is used:

$$c_{\text{data}} = \sqrt{2 \cdot \left(\left(\frac{\sigma}{m_Z} \right)_{\text{data}}^2 - \left(\frac{\sigma}{m_Z} \right)_{\text{MC}}^2 \right) + c_{\text{MC}}^2}$$

where c_{MC} is the constant term in simulation, while m_Z denotes the Z mass and σ the Gaussian component of the experimental resolution, obtained by fitting with a Breit-Wigner convolved with a Crystal Ball function [16], [17]. Recent results for all η -ranges are shown in Table I.

Finally, the electron energy response stability is demonstrated with respect to time (Fig. 19) as well as the LHC pileup conditions (Fig. 20) by studying the evolution of the peak of the invariant mass distribution in $Z \rightarrow ee$ events and the most probable value of the E/p ratio in $W \rightarrow e\nu$ events, with respect to a reference value. The stability in 2012 is excellent,

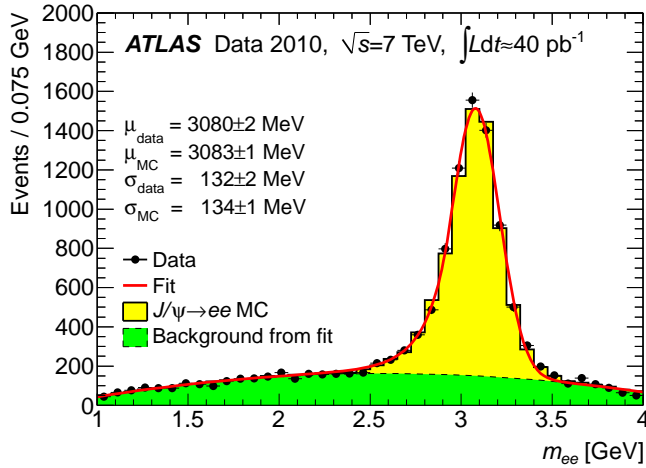


Fig. 18. Reconstructed dielectron mass distribution for $J/\psi \rightarrow ee$ decays and comparison to simulation [15].

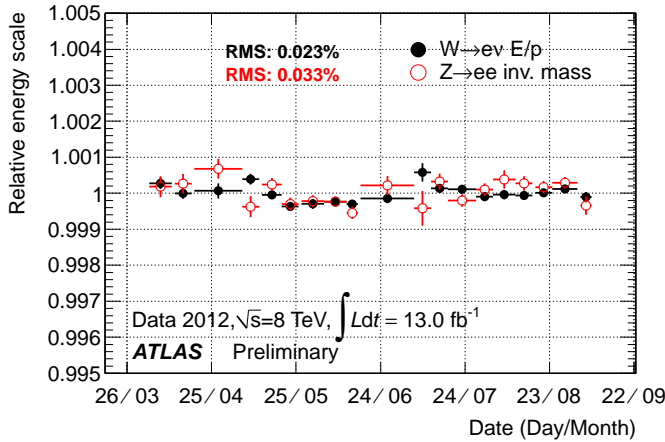


Fig. 19. Electron energy response stability with time in 2012 data [18].

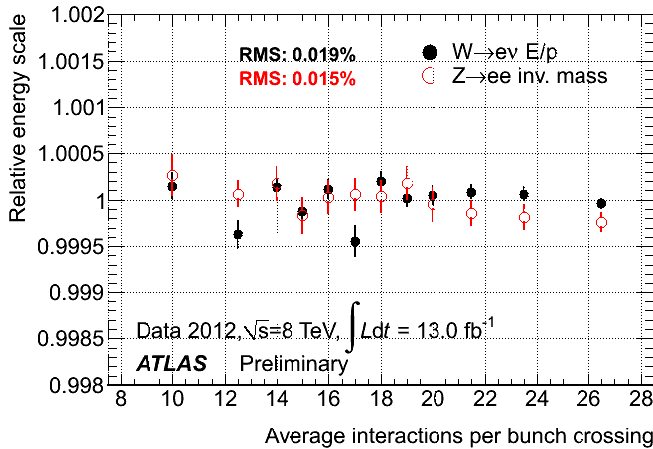


Fig. 20. Electron energy response stability with pileup (average number of interactions per bunch crossing) in 2012 data [19].

better than 0.03% which is expected for a LAr calorimeter with stable temperature and purity conditions.

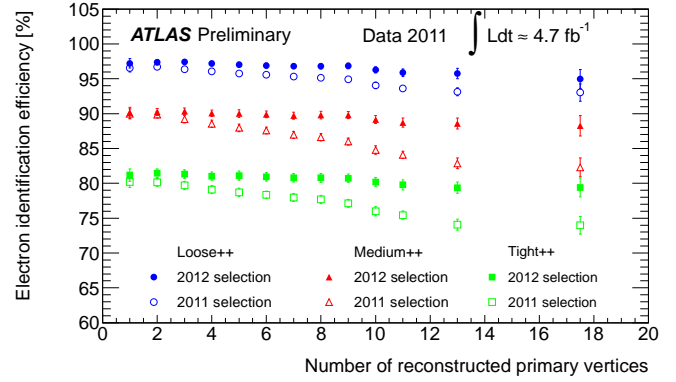


Fig. 21. Dependence of electron identification efficiency on pileup, measured using $Z \rightarrow ee$, $J/\psi \rightarrow ee$ and $W \rightarrow e\nu$ events [21].

B. Identification Efficiency

In addition to having good resolution and uniformity, the calorimeter is required to have excellent electron/photon identification efficiency and a high jet rejection rate over a broad energy range. The fine segmentation of the LAr calorimeter makes this possible by providing valuable information for the shape and other characteristics of the EM showers. In addition, photons which leave no tracks in the ID can be efficiently detected and their direction measured using the same feature. More specifically, the photon flight direction can be reconstructed by measuring precisely the position of the cluster barycenters in the first and second LAr calorimeter layers in depth.

In ATLAS, electron identification [20] is performed with a cut-based method combining information from the shower shape characteristics in the calorimeter with the information from the ID where available. Three reference sets of cuts have been defined with increasing background rejection power: *loose*, *medium* and *tight* with an expected jet rejection of approximately 500, 5000 and 50000, respectively, based on MC simulation. The values of the cuts are optimized according to the beam conditions, leading to an improved set of cuts for 2012 which performs better in high pileup conditions while maintaining similar jet rejection power. As can be seen in Fig. 21, an identification efficiency exceeding 95%, 88% and 79% is achieved in 2012 for *loose*, *medium* and *tight* respectively, for up to 20 reconstructed primary vertices per event.

Photon reconstruction [23] is similar to electrons albeit more involved due to the fact that photons can be either unconverted or converted. The latter are characterized by the presence of at least one track in the ID that matches the EM cluster in the calorimeter, resulting in an ambiguity in the distinction between converted photons and electrons. In addition, unconverted photons can also be reconstructed as electrons if their EM clusters are erroneously associated with tracks that typically have low momentum. For this reason, a procedure has been established to recover photon candidates from a collection of electron candidates, based on combined information from the ID and the calorimeter (number and momentum of matched tracks, number and position of hits in the ID, E/p ratio). To provide a pure photon sample and

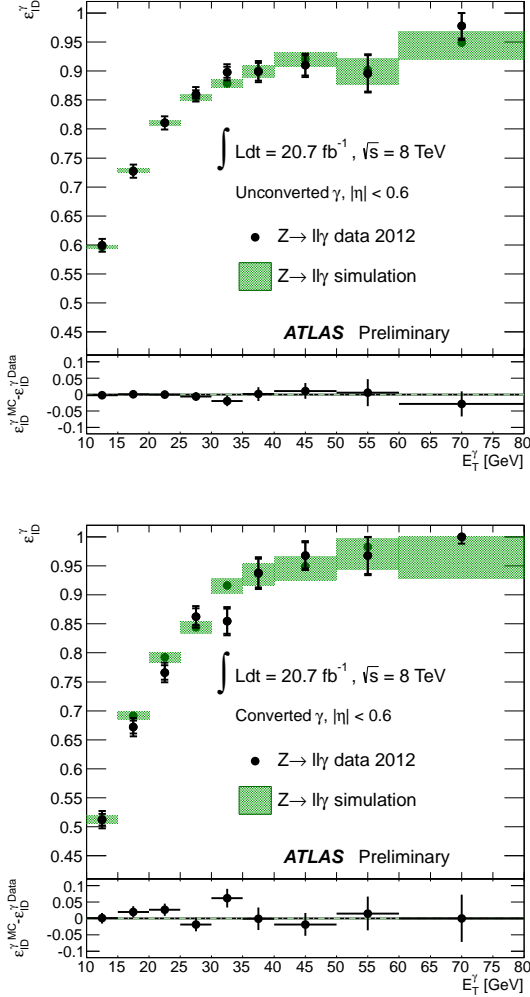


Fig. 22. Photon identification efficiency for unconverted (top) and converted (bottom) photon candidates obtained in $Z \rightarrow \ell\ell\gamma$ events, for $|\eta| < 0.6$. Similar performance is observed in other η ranges [22].

study the photon identification efficiency, the radiative Z decay $Z \rightarrow \ell\ell\gamma$ is exploited [22], where the lepton ℓ , can be an electron or a muon. In these studies, no requirements on the photon shower shape are applied, to avoid any bias. As shown in Fig. 22, the efficiency is very high for both converted and unconverted candidates, and agrees with the expected performance from MC simulation.

The fine granularity of the calorimeter is a significant asset allowing the separation of photons from jets. As can be seen in Fig. 23, the shower shape for a photon is expected to have a narrower profile compared to the shower shape for a jet. Especially in the presence of a π^0 meson, a distinctive energy deposition with two energy maxima is expected in the first layer of the LAr calorimeter (strips). To efficiently reject background in analyses using photons, photon identification is performed, similarly to electrons, using the characteristics of their shower shape. Two reference sets of cuts, *loose* and *tight*, are defined. The former set of cuts has a very high efficiency with a modest jet rejection power, while the latter has a rejection power of approximately 5000 while keeping a

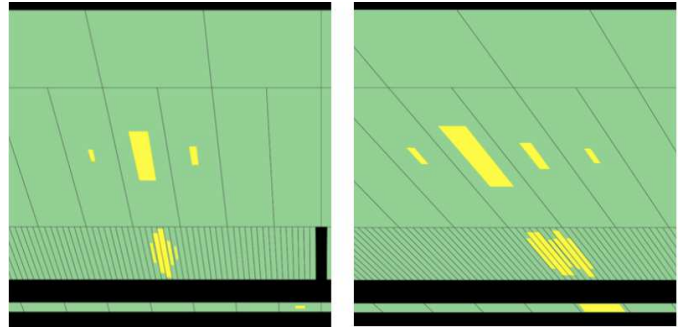


Fig. 23. Shower shapes for a photon candidate (left) and a candidate for a jet with a leading π^0 (right), in data recorded in proton-proton collisions [25].

relatively high efficiency, approximately 85% for photons with transverse energy $E_T > 40$ GeV [24].

C. The Discovery of a Higgs-Like Boson in ATLAS

A high functionality of all detector components is required for all ATLAS physics analyses. Especially in the case of searches for new physics, the efficient running of the detector as a whole is imperative for the rapid accumulation of data delivered by the LHC. As described in previous sections, the LAr calorimeter operated close to optimally over the last three years, contributing to the very high ATLAS overall efficiency which culminated in the discovery [26] of a Higgs-like boson in July 2012. By providing efficient identification and precise measurement of electrons and photons, the LAr calorimeter was invaluable in the search for the Higgs boson especially in its decay channels $H \rightarrow 2\mu 2e$, $H \rightarrow 4e$ [27] and $H \rightarrow \gamma\gamma$ [28].

In the search for the Higgs decay to two photons, the LAr calorimeter played an especially significant role. In brief, the $H \rightarrow \gamma\gamma$ analysis searches the diphoton invariant mass spectrum for a small excess over a formidable background (Fig. 24). As described in Section V-B, the calorimeter provides excellent photon identification and jet background rejection, by exploiting its fine longitudinal segmentation, thereby improving the signal to background ratio. Further, the diphoton invariant mass, defined as

$$m_{\gamma\gamma} = \sqrt{2E_1E_2(1 - \cos\theta)}$$

where E_1 , E_2 are the two photon energies and θ is the angle between them, needs to be reconstructed with a very high precision so a very small excess can be distinguished over a large background. With an excellent energy resolution, the calorimeter ensures a very good measurement of the photon energies. In addition, the unique capability to reconstruct the photon direction is a significant advantage in improving the angle measurement in the high pileup environment of the LHC. More specifically, the calorimeter pointing is used to choose the event primary vertex (PV) from a set of several tens of PV candidates. As shown in Fig. 25, the use of the calorimeter information, labeled as “Calo pointing” is significantly better than the ID-only approach, labeled as “Max $\sum p_T^2$ ”, which selects the PV based on the momentum of the tracks associated with each candidate. Further, it is very similar to the optimal

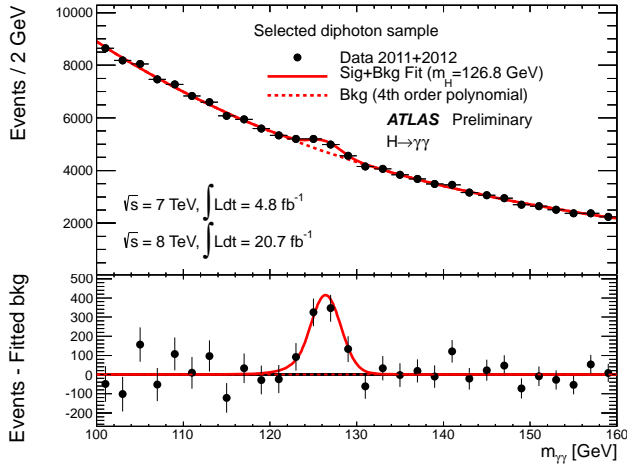


Fig. 24. Invariant mass distribution of diphoton candidates for the combined $\sqrt{s} = 7$ TeV and $\sqrt{s} = 8$ TeV data samples. The result of a fit to the data of the sum of a signal component fixed to $m_H = 126.8$ GeV and a background component described by a fourth-order Bernstein polynomial is superimposed. The bottom inset displays the residuals of the data with respect to the fitted background component [28].

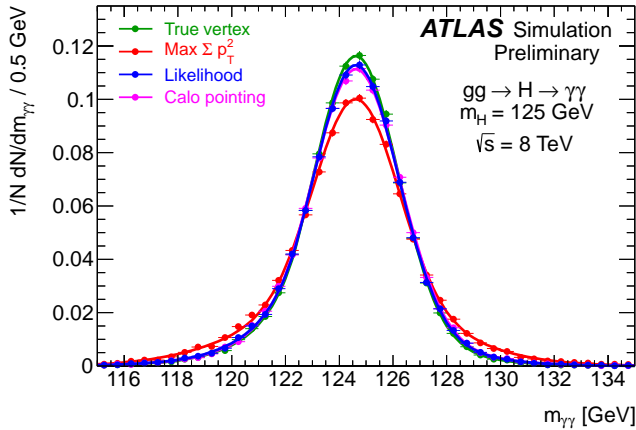


Fig. 25. Distribution of the expected diphoton mass for $H \rightarrow \gamma\gamma$ signal events as a function of the algorithm used to determine the longitudinal vertex position of the hard-scattering event [29].

achievable mass resolution labeled as “True vertex”. Finally, the “Likelihood” method combines this information with the primary vertex information from the tracking and provides similar mass resolution. With the PV position known with high precision from the ID, the angle between the two photons is calculated with a very good resolution, which translates to an excellent invariant mass resolution.

VI. UPGRADE PLANS

The High Luminosity (HL) LHC intends to extend and improve the LHC program beyond 2022, by operating with an instantaneous luminosity up to 5 times the original design luminosity of $10^{34} \text{ cm}^{-2}\text{s}^{-1}$. Already by 2012, the LHC has been operating very close to the design luminosity and after the ongoing shutdown (LS1), in 2015 it is intended to exceed it. After an additional shutdown period in 2018 (LS2), the accelerator chain will be upgraded so the LHC can reach a

luminosity of $3 \times 10^{34} \text{ cm}^{-2}\text{s}^{-1}$. A road map has been set to upgrade the calorimeter in two phases, as the HL-LHC era approaches, to maintain a high level of performance in these harsh conditions.

In Phase-1 [30], during LS2, the calorimeter L1 trigger will be upgraded to cope with the high rates expected. Given a limited bandwidth allowance, it is otherwise required to either raise the trigger thresholds or randomly discard interesting events, neither of which is desired. The proposed solution is to upgrade the existing trigger electronics with a new front-end LAr Trigger Digitizer Board and additional back-end electronics. In this architecture, the coarse granularity trigger towers will be complemented with finer granularity “super-cells”. In addition, it will be possible to perform complex shower shape calculations at the hardware level. These new features allow better rejection of undesired background events online using characteristics of the shower shape, in a similar way as is done in physics analyses offline, therefore saving the bandwidth for more interesting events.

For the Phase-2 upgrade [31], the front-end electronics will move to a fully digital architecture [32] and will take advantage of the technology developed for the Phase-1 trigger upgrade. In the proposed architecture, the signal will be digitized continuously at the 40 MHz LHC clock frequency and transmitted to an off-detector back-end system able to handle readout at 150 TBps. At the back-end, input will be provided to a new fully-digital L1 trigger system. It is also proposed to use the trigger upgrades from Phase-1 to create an additional, lower level for triggering, dubbed Level-0.

Finally, in the HL-LHC environment, degradation of the FCal performance is expected [33]. The increased particle fluxes will have the following effects to FCal operation: First, at high ionization rates, space-charge effects become significant, when the positive argon ions build up in the LAr and distort the electric field. Secondly, the high currents expected will cause a large voltage drop over the HV protection resistors in place to protect the system from arcing. Both these effects degrade the signal measurement. Finally, the large rates and currents may generate heat to the level that can boil the LAr which is of course undesirable.

A first option is to replace the current FCal modules with ones able to withstand the higher fluxes anticipated. The new modules would feature smaller LAr gaps to solve the space-charge issue while the value of the protective resistors would be reduced to avoid a significant voltage drop with the currents expected. Finally, they would employ liquid nitrogen cooling loops to remove the excess heat. This option would require the opening of the cryostat which is projected to be a challenging and risky operation. This solution would therefore be especially considered should there be a particular need to open the cold vessel. For example, unlike the other LAr subsystems, the HEC employs cold GaAs pre-amplifiers that are located inside the endcap cryostats in LAr. Studies are underway to determine whether the HEC cold electronics will need to be replaced for HL-LHC, in which case the FCal will need to be removed from the cryostat to allow access to the HEC. Due to activation of the FCal, it will not be possible to re-install it after the HEC intervention, without exposing the

personnel to unacceptable radiation levels. In this scenario, therefore, complete replacement of the modules is favored.

A second option would consist of installing an additional warm calorimeter (named *miniFCal*) in available space in front of the existing FCal system, closer to the interaction point. This option is attractive since it avoids the risk of opening the cryostat cold volume and can be installed more readily, thereby saving time. Various technologies have been proposed for the *miniFCal*. One of them, very radiation hard, involving diamond wafers as active material, has been studied to assess its linearity, uniformity and resolution. However, this option is disfavored mainly due to its prohibiting cost. Other considered technologies include xenon gas as active medium as well as familiar LAr technology, each with their own implementation challenges.

Finally there is the option of not taking any action and living with the degraded performance and the possibility of the LAr boiling at very high rates, which has yet to be explicitly ruled out. Additional studies are required to better quantify the level of FCal degradation to be anticipated in HL-LHC, before a decision is made taking into account detector safety, schedule and cost.

VII. CONCLUSION

The LAr calorimeter system has performed exceptionally well over the first few years of operation, with near optimal efficiency as well as impressive performance, contributing to the overall ATLAS performance that culminated in the discovery in 2012 of the long sought after Higgs boson. Keeping this level of performance requires a tremendous effort by a significant number of people who intend to keep or exceed this level in the coming challenging years. Studies are continuing in order to improve the performance as the LHC delivers data at unprecedented energies and rates, and ensure that any physics that exists at the TeV-scale will be discovered.

REFERENCES

- [1] G. Aad *et al.*, “The ATLAS experiment at the CERN Large Hadron Collider,” *JINST*, vol. 3, p. S08003, 2008.
- [2] B. Aubert *et al.*, “Construction, assembly and tests of the ATLAS electromagnetic barrel calorimeter,” *Nucl.Instrum.Meth.*, vol. 558, no. 2, pp. 388 – 418, 2006.
- [3] M. Aleksa *et al.*, “Construction, assembly and tests of the ATLAS electromagnetic end-cap calorimeters,” *JINST*, vol. 3, no. 06, p. P06002, 2008.
- [4] D. M. Gingrich, “Construction, assembly and testing of the ATLAS hadronic end-cap calorimeter,” *JINST*, vol. 2, no. 05, p. P05005, 2007.
- [5] A. Artamonov *et al.*, “The ATLAS Forward Calorimeter,” *JINST*, vol. 3, p. P02010, 2008.
- [6] G. Aad *et al.*, “Drift time measurement in the ATLAS Liquid Argon Electromagnetic Calorimeter using cosmic muons,” *Eur.Phys.J.*, vol. C70, pp. 755–785, 2010.
- [7] N. J. Buchanan *et al.*, “ATLAS Liquid Argon calorimeter front end electronics,” *JINST*, vol. 3, no. 09, p. P09003, 2008.
- [8] W. E. Cleland and E. G. Stern, “Signal processing considerations for liquid ionization calorimeters in a high rate environment,” *Nucl.Instrum.Meth.*, vol. A338, pp. 467–497, 1994.
- [9] ETM professional control at <http://www.etm.at>.
- [10] Public LAr calorimeter plots on detector status at <https://twiki.cern.ch/twiki/bin/view/AtlasPublic/LArCaloPublicResultsDetStatus>.
- [11] M. Adams *et al.*, “A purity monitoring system for liquid argon calorimeters,” *Nucl.Instrum.Meth.*, vol. A545, pp. 613–623, 2005.
- [12] Public LAr calorimeter plots for collision data at <https://twiki.cern.ch/twiki/bin/view/AtlasPublic/LArCaloPublicResults2010>.
- [13] “Non-collision backgrounds as measured by the atlas detector during the 2010 proton-proton run,” CERN, Geneva, Tech. Rep. ATLAS-CONF-2011-137, Sep 2011.
- [14] G. Aad *et al.*, “Search for non-pointing photons in the diphoton and E_{T}^{miss} final state in $\sqrt{s} = 7$ TeV proton-proton collisions using the ATLAS detector,” Apr 2013, submitted to Phys. Rev. D.
- [15] —, “Electron performance measurements with the ATLAS detector using the 2010 LHC proton-proton collision data,” *Eur. Phys. J.*, vol. C72, p. 1909, 2012.
- [16] M. J. Oreglia, “A study of the reactions $\psi' \rightarrow \gamma\gamma\psi$,” *Ph. D thesis*, 1980, Appendix D.
- [17] J. E. Gaiser, “Charmonium spectroscopy from radiative decays of the J/ψ and ψ' ,” *Ph. D thesis*, 1982, Appendix F.
- [18] “Electron energy response stability with time up to september 2012 (hcp dataset),” CERN, Geneva, Tech. Rep. ATL-COM-PHYS-2012-1593, Nov 2012.
- [19] “Electron energy response with respect to pileup in 2012 data,” CERN, Geneva, Tech. Rep. ATL-COM-PHYS-2012-1668, Nov 2012.
- [20] “Expected electron performance in the ATLAS experiment,” CERN, Geneva, Tech. Rep. ATL-PHYS-PUB-2011-006, Apr 2011.
- [21] “Electron identification efficiency dependence on pileup,” CERN, Geneva, Tech. Rep. ATL-COM-PHYS-2011-1636, Nov 2011.
- [22] “Photon identification efficiency measurements using $Z \rightarrow \ell\ell\gamma$ events in 20.7 fb^{-1} of pp collisions collected by atlas at $\sqrt{s} = 8 \text{ tev}$ in 2012,” CERN, Geneva, Tech. Rep. ATL-COM-PHYS-2013-244, Feb 2013.
- [23] “Expected photon performance in the ATLAS experiment,” CERN, Geneva, Tech. Rep. ATL-PHYS-PUB-2011-007, Apr 2011.
- [24] “Measurements of the photon identification efficiency with the ATLAS detector using 4.9 fb^{-1} of pp collision data collected in 2011,” CERN, Geneva, Tech. Rep. ATLAS-CONF-2012-123, Aug 2012.
- [25] Electron/Gamma public results at <https://atlas.web.cern.ch/Atlas/GROUPS/PHYSICS/EGAMMA/PublicPlots/20100721/display-photons/display-photons.pdf>.
- [26] G. Aad *et al.*, “Observation of a new particle in the search for the Standard Model Higgs boson with the ATLAS detector at the LHC,” *Phys.Lett.*, vol. B716, pp. 1–29, 2012.
- [27] “Measurements of the properties of the Higgs-like boson in the four lepton decay channel with the ATLAS detector using 25 fb^{-1} of proton-proton collision data,” CERN, Geneva, Tech. Rep. ATLAS-CONF-2013-013, Mar 2013.
- [28] “Measurements of the properties of the Higgs-like boson in the two photon decay channel with the ATLAS detector using 25 fb^{-1} of proton-proton collision data,” CERN, Geneva, Tech. Rep. ATLAS-CONF-2013-012, Mar 2013.
- [29] “Observation of an excess of events in the search for the Standard Model Higgs boson in the gamma-gamma channel with the ATLAS detector,” CERN, Geneva, Tech. Rep. ATLAS-CONF-2012-091, Jul 2012.
- [30] “Letter of intent for the Phase-I upgrade of the ATLAS experiment,” CERN, Geneva, Tech. Rep. CERN-LHCC-2011-012. LHCC-I-020, Nov 2011.
- [31] “Letter of intent for the Phase-II upgrade of the ATLAS experiment,” CERN, Geneva, Tech. Rep. CERN-LHCC-2012-022. LHCC-I-023, Dec 2012.
- [32] Timothy R Andeen, “Upgraded Readout Electronics for the ATLAS Liquid Argon Calorimeters at the High Luminosity LHC,” *Journal of Physics: Conference Series*, vol. 404, no. 1, p. 012061, 2012.
- [33] J. Rutherford, “Upgrade plans for the ATLAS Forward Calorimeter at the HL-LHC,” *Journal of Physics: Conference Series*, vol. 404, no. 1, p. 012015, 2012.